Nanoscale

PAPER

View Article Online
View Journal

Cite this: DOI: 10.1039/d5nr03812j

Self-folding graphene scaffolds with integrated electronics for cardiac tissue engineering

Alonso Ingar Romero, [a,b,c,g] Koji Sakai, [c,d] Toichiro Goto, [c,d] George Al Boustani, [a,b,g] Ryuya Kida, [a,b,g] Defne Tüzün, [a,b,g] Yuta Tanimura, [b] Ann-Caroline Heiler, [e,f,g] Joe Alexander, [a] Andreas R. Bausch, [e,f,g] Bernhard Wolfrum [a,b,g] and Tetsuhiko F. Teshima *[a,b,g,h]

Three-dimensional (3D) cardiac microtissues offer physiologically relevant platforms for studying cardiac development, disease modelling, and drug screening. Scaffold-based strategies, particularly those incorporating graphene, have shown promise in supporting cardiomyocyte alignment, maturation, and contractility due to graphene's high electrical conductivity, mechanical flexibility, and biocompatibility. In addition, effective bioelectronic interfacing is essential for capturing electrophysiological dynamics and modulating cardiac function in engineered tissues. However, current methods typically separate tissue scaffolding from bioelectronic interfacing, limiting integration efficiency and signal fidelity. Here, we report a self-folded graphene micro-roll platform that simultaneously functions as a 3D scaffold and integrated electrical interface. Each micro-roll embeds 4 graphene-based microelectrodes, enabling real-time electrophysiological monitoring and localised stimulation without external probes. Cardiomyocytes seeded onto the micro-rolls spontaneously assembled into tissue conforming to the scaffold geometry, supporting synchronous contraction and exhibiting stimulation-induced modulation of the beating frequency. This system provides a practical, scalable approach to creating electrically active cardiac constructs with promising applications in tissue engineering, disease research, and drug development.

Received 10th September 2025,
Accepted 30th April 2026

DOI: 10.1039/d5nr03812j

rsc.li/nanoscale

Introduction

Three-dimensional (3D) cardiac microtissues have become essential tools for studying heart development, modelling disease, and evaluating drug responses *in vitro*.[1–3] By mimicking the structural and mechanical cues of the native myocardium, 3D constructs promote more physiologically relevant behaviour than traditional two-dimensional (2D) monolayers, enabling improved cardiomyocyte alignment, contractility, and maturation.[4,5] Techniques for fabricating 3D cardiac microtissues generally fall into two categories: scaffold-based methods, which employ natural or synthetic materials to provide a structural framework, and scaffold-free methods, such as spheroid formation or cell-sheet engineering, which rely on self-assembly and organisation through cellular adhesion.[6] Among these, scaffold-based approaches offer enhanced architectural control and mechanical support, which are critical for mimicking the anisotropic and contractile behaviour of cardiac tissue.[7] In addition, the capacity to electrically monitor and modulate cardiomyocyte behaviour is crucial for characterising functional development, pathologies, and pharmacological responsiveness.[8–11] Electrical monitoring through microelectrode arrays (MEAs) and field stimulation techniques have been extensively used in monolayer and 3D cardiac cultures to capture action potentials, conduction velocity, and synchronous contraction.[12,13] Controlled electrical pacing further enhances cardiomyocyte alignment, gap junction formation, functional maturation, and pharmacological response.[14,15] Several studies have required physical manipulation or external force to bring 3D tissues into contact with electrodes and other sensors, a process that risks introducing mechanical stress or altering tissue morphology.[16–18] In contrast, direct electrode integration within the scaffold can improve

[a]*Medical & Health Informatics Laboratories, NTT Research Incorporated, Sunnyvale, CA, 94085, USA. E-mail: tetsuhiko.teshima@ntt-research.com*
[b]*Neuroelectronics Lab, Munich Institute of Biomedical Engineering, Department of Electrical Engineering, TUM School of Computation, Information and Technology, Technical University of Munich, Garching, Germany*
[c]*Basic Research Laboratories, NTT, Inc., 3-1 Morinosato Wakamiya, Atsugi, Kanagawa 243-0198, Japan*
[d]*NTT Bio-Medical Informatics Research Center, NTT, Inc., 3-1 Morinosato Wakamiya, Atsugi, Kanagawa 243-0198, Japan*
[e]*Heinz Nixdorf Chair in Biophysical Engineering of Living Matter, Garching, Germany*
[f]*Center for Functional Protein Assemblies (CPA), Technical University of Munich, Garching, Germany*
[g]*Center for Organoid Systems (COS), Technical University of Munich, Garching, Germany*
[h]*Department of Mechanical Engineering, Faculty of Science and Technology, Keio University, 3-14-1 Hiyoshi, Kohoku-ku, Yokohama, 223-8522, Japan*

signal coupling and eliminate the need for complex positioning steps. Some approaches to achieve this involve, for example, embedding pillars or mesh electronics into a scaffolding material.[19–21]

Recently, graphene-based materials have emerged as particularly attractive scaffold materials for cardiac applications and tissue engineering in general.[22,23] Due to their unique combination of high electrical conductivity and biocompatibility, graphene-based substrates and composites have shown to enhance cardiomyocyte adhesion, sarcomeric organisation, and spontaneous contraction.[24–26] In particular, the out-of-plane flexibility and in-plane stiffness of monolayer graphene make it suitable for building robust 3D structures, for example, based on self-folding mechanisms.[27–29] Beyond passive scaffolding, graphene's high electrical conductivity and mechanical flexibility also make it an attractive candidate for developing bioelectronic interfaces, including microelectrodes and sensing elements, enabling low-noise, high-resolution recording of electrophysiological signals in electroactive tissues, in both 2D and 3D environments.[30–37] This dual functionality—3D mechanical support and electrical interface—suggests that graphene could serve as a multifunctional material, enabling a seamless integration of structural scaffolding and electrical communication within a single platform. Such a configuration would be particularly valuable in engineered cardiac tissues, where synchronised electrical signalling is critical for functional tissue maturation and where integrated sensing or pacing capabilities could enhance tissue monitoring or control. Despite this potential, no existing cardiac tissue culture platform has successfully used graphene in this dual role. Current approaches typically rely on separate materials for scaffolding and electrode function, which can introduce mechanical mismatches, complicate fabrication, and limit spatiotemporal resolution of stimulation or recording. Therefore, there is a need for an integrated platform that utilises graphene simultaneously as a scaffold and as an embedded electrode array.

Here, we present a self-folded graphene micro-roll platform that integrates electrodes directly into the 3D scaffold architecture. Each micro-roll contains 4 graphene-based microelectrodes, enabling direct electrical access to the tissue without the need for external probes. Unlike flat or mesh-based systems, the rolled architecture facilitates circumferential alignment, enhances tissue anchoring, and enables spatially distributed electrical interfacing within a physiologically relevant microenvironment. Primary neonatal rat cardiomyocytes seeded onto the micro-rolls spontaneously assembled into aggregates conforming to the 3D geometry, confirming the ability of the micro-roll structure to support self-organisation of cardiomyocytes into tissue-like structures. Moreover, the embedded electrodes enable stable electrophysiological recordings and stimulation-induced modulation of the cardiac network activity. To further characterise the electro-performance and show the versatility of our platform, we used HL-1 cardiac muscle cell line (mouse) and human induced pluripotent stem cell-derived cardiomyocytes (hiPSC-CMs). This modular, scalable system bridges the gap between scaffold design and bioelectronic interfacing of graphene-based platforms, offering a versatile tool for cardiac tissue engineering and laying the foundation for future applications in disease modelling and pharmacological studies.

Experimental

Fabrication of self-foldable graphene electrodes

Fig. 1a illustrates the fabrication process of self-folding graphene electrodes. A Cr/Au layer was thermally deposited on glass substrates (0.5 mm thick, 50 × 50 mm^2, and 1 mm thick, 49 × 49 mm^2; both from Matsunami, used for different MEA systems), followed by spin-coating and photo-lithographical patterning of positive photoresist (MICROPOSIT S1813G, MICROPOSIT 351). The Cr and Au films were then etched to form feedlines by a ceric ammonium nitrate-based Cr etchant (Sigma-Aldrich) and an iodide-based Au etchant (Kanto Chemical), respectively (i). After washing the remaining photoresist with acetone, a 2 wt% Na-alginate solution (A2033, Sigma-Aldrich) was spin-coated onto the feedlines at a peak speed of 2000 rpm for 30 s, yielding a layer thickness of approximately 60 nm. This alginate layer served as a sacrificial material for later detachment of the structure. The wafers were then submerged in a 100 mM $CaCl_2$ solution (C8106, Sigma-Aldrich) to induce gelation of the Ca-alginate. 6 wt% polymethylmethacrylate (PMMA, 950 Kayaku) in anisole was spin-coated on the Ca-alginate at 3000 rpm for 40 s to protect it from the alkaline developer during the next photolithography step. After spin coating and patterning a positive photoresist mask, the PMMA and Ca-alginate layers were structured using reactive ion etching (RIE) with O_2 plasma to create an array of square films (ii). This allows the Ca-alginate to be present only in the areas needed, while leaving the feedlines exposed to ensure proper contact with graphene. Fig. S1 shows the height profile measurement of the patterned Ca-alginate pads. After washing the photoresist and PMMA with acetone, 7 × 7 mm^2 monolayer graphene films (CVD-grown on Cu foils, Sigma Aldrich) were transferred onto the samples using the conventional chemical etchant-assisted wet transfer technique.[38] Specifically, graphene was first coated with a PMMA layer and then transferred by dissolving the Cu substrates using 45% $FeCl_3$ solution (Sigma-Aldrich). After the transferring process, the PMMA coating was eliminated by immersing the sample in acetone (iii). The individual graphene electrodes were patterned *via* another photolithography process and a brief RIE exposure with O_2 plasma (iv). Fig. S2 shows the measured height profile of the patterned graphene surface. Next, the samples were coated with ~120 nm parylene-C using CVD (SCS LABCOATER PDS2010) (v). During deposition, dichloro-di(*p*-xylylene) (SCS) was vapourised at 150 °C and subsequently pyrolysed at 690 °C to produce a chloro-*p*-xylylene monomer, which was then deposited onto the graphene surface to form a uniform membrane of polymerised chloro-*p*-xylylene, called parylene-C.

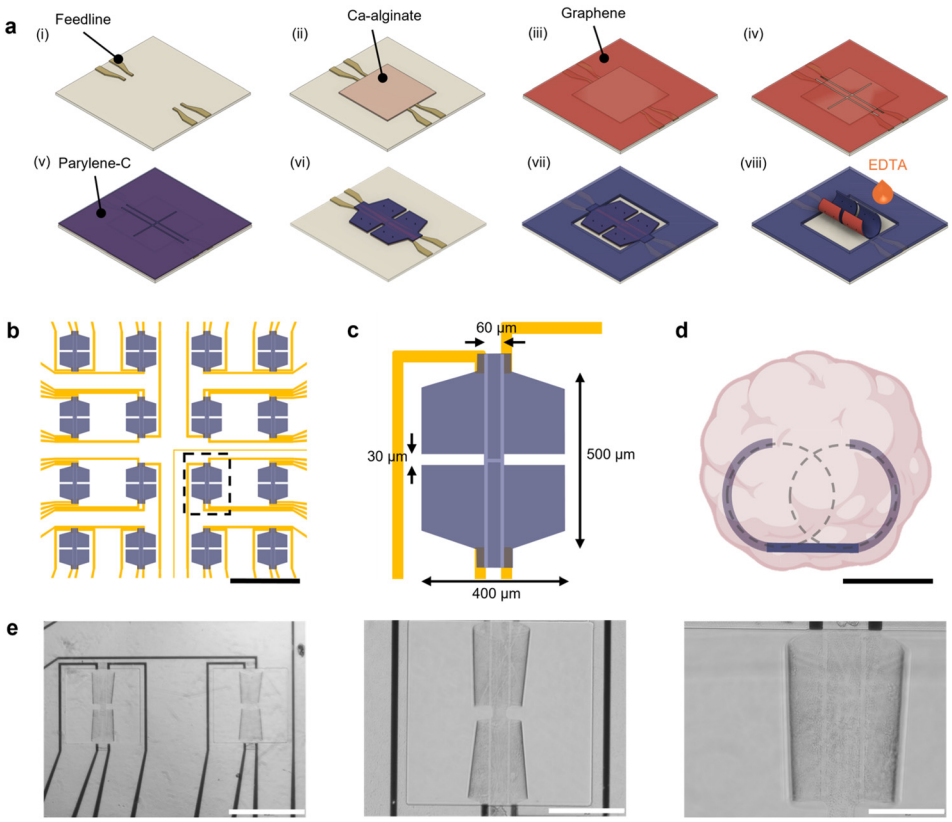

Fig. 1 Design, fabrication process, and final geometry of the graphene-based micro-roll scaffolds. (a) Fabrication scheme of the graphene micro-roll electrodes. (b) Top-view layout of the planar microelectrode array layout before self-folding. (c) Detailed design of a single graphene micro-roll electrode with annotated dimensions corresponding to the highlighted area in (b). (d) Front-view representation of a cardiac tissue aggregate encapsulating a single graphene micro-roll. The dashed circles represent the two tubular structures used to model the device architecture. (e) Phase-contrast microscopy images of the self-folded micro-rolls at 4× (left), 10× (centre), and 20× magnification (right). Scale bars: (b) 1 mm, (d) 100 μm, (e) From left to right 500 μm, 200 μm and 100 μm.

We utilised photolithography to pattern a trilayer comprising Ca-alginate, parylene-C, and graphene into individual micro-rolls. The triple-layered film was first coated with S1813G, serving as a hard mask. The S1813G photoresist was micropatterned on the parylene-C surface through photolithography, providing protection during the subsequent RIE steps. The layers were then etched using RIE with O_2 plasma to produce a micropatterned film array (vi). The feedlines were then passivated by a 1.5 μm parylene-C film according to previously reported protocols (vii).[39] Finally, the arrays were released from the SiO_2 wafer by immersing them in an aqueous 0.5 M Ethylenediaminetetraacetic acid (EDTA) solution (Thermo Fisher Scientific) (viii).[40] For cell culture, a glass ring (20 mm in diameter) was affixed to the substrate to form a reservoir for the culture medium. To bond the ring, the edge was coated with polydimethylsiloxane (PDMS; Silpot 184, Dow Corning Toray) prepolymer. The glass ring was then positioned at the centre of the substrate, and the PDMS was cured at 80 °C for 2 h.

In total, the fabrication process involved 4 sequential photolithography steps (metal feedlines, sacrificial Ca-alginate, micro-roll patterning, and parylene-C passivation), as well as one maskless alignment for graphene patterning. For the cumulative alignment tolerance across all layers, our process is estimated to be within 2 μm. Given that the feedline width and inter-electrode spacing exceed 20 μm, this corresponds to less than 10% of the critical dimension. This estimate agrees with optical microscopy inspection of representative samples, which showed no visible interlayer displacement at 20× magnification.

Electrochemical analysis of 2DLM micro-rolls

Cyclic voltammetry (CV) and electrochemical impedance spectroscopy (EIS) were performed to characterise the graphene electrodes using a potentiostat (VSP-300, Bio-Logic Science Instruments). Both measurements were carried out at room temperature using phosphate-buffered saline (Modified Dulbecco's PBS, Sigma-Aldrich) as the electrolyte. A 3-electrode setup was used, consisting of an Ag/AgCl (3 M NaCl) reference electrode and a Pt wire counter electrode. CV measurements were conducted over a potential window of −0.7 to 0.7 V *vs.* Ag/AgCl at a scan rate of 100 mV s^{-1}. For EIS, a 10 mV sinusoidal signal (relative to the open-circuit potential) was applied, and impedance was recorded across a frequency range of 1 to 10^4 Hz.

To evaluate the electrochemical stability of the electrodes during stimulation, biphasic pulses of ±50 μA with a phase duration of 100 μs were applied at 100 Hz using the MEA2100-Mini-System (Multichannel Systems). The electrode voltage response to biphasic current pulses was recorded using an oscilloscope (InfiniiVision DSOX2024A, Keysight). Current stimulation was delivered *via* an electrophysiology stimulator/amplifier chip (RHS2116, Intan Technologies) within the 3-electrode setup described above. Each pulse consisted of a 100 μs phase (leading cathodic) followed by a 100 μs inter-phase delay. The pulse amplitude was varied from 10 to 100 μA in increments of 10 μA.

Cell culture

Primary cardiomyocytes were isolated from the cardiac tissues of 1–3-day-old neonatal Wistar rat embryos (Jackson Laboratory).† The cardiac tissue was enzymatically dissociated into single cells using collagenase and trypsin. The resulting cell suspension was seeded onto the chips with a concentration of around 2.5 Mio. cm^{-2} in Dulbecco's Modified Eagle Medium (DMEM; Thermo Fisher Scientific) supplemented with 10% fetal bovine serum (FBS; Thermo Fisher Scientific) and 1% penicillin–streptomycin (Corning). Before cell seeding, the self-folded graphene electrodes were coated with a 50 μg mL^{-1} fibronectin solution (Thermo Fisher Scientific) for 1 h.

HL-1 cells were cultured in Claycomb medium (Sigma-Aldrich) supplemented with 100 U mL^{-1} penicillin, 100 μg mL^{-1} penicillin–streptomycin, 2 mM L-glutamine, 10% fetal bovine serum, and 0.1 mM norepinephrine (ThermoFisher Scientific) in a cell culture flask. Upon reaching confluency, the cells were detached using a 0.05% trypsin–EDTA solution (Sigma-Aldrich) and prepared for experimentation. Before cell seeding, the devices were incubated with a fibronectin (5 μg mL^{-1}) and gelatin (0.2 mg mL^{-1}) solution for approximately 1 h at 37 °C. HL-1 cells were seeded onto the chips with a concentration of 200k cm^{-2}, reaching confluency in about 2 days. hiPSC-CMs were obtained following the GSK3 inhibitor and Wnt inhibitor (GiWi) differentiation protocol,[41] adapted as described in previous works.[42] All the cultures were maintained in a CO_2 incubator (5%; 37 °C; humidified air) except during the electrophysiological experiments.

SEM

For SEM imaging, the samples were fixed by replacing the culture medium with a solution of 2% glutaraldehyde (FUJIFILM Wako Chemicals) in PBS for 30 min. Following fixation, the solution was gradually substituted with ethanol through a series of stepwise exchanges using ethanol–water mixtures. This was followed by replacement with *tert*-butyl alcohol (Sigma-Aldrich), and the samples were then freeze-dried overnight. After drying, a 10 nm Au layer was sputter-coated onto the samples. Imaging was conducted using a FIB-SEM system (Auriga 60 Cross Beam Workstation, Carl Zeiss) at an accelerating voltage of 5 kV.

Immunostaining

To prepare the samples for immunostaining, the culture medium was replaced with 4% paraformaldehyde (PFA, Sigma-Aldrich) in PBS and incubated at room temperature for 30 min. After fixation, the PFA solution was carefully removed and replaced with a blocking buffer containing 1% bovine serum albumin (BSA, Thermo Fisher Scientific) and 0.1% Triton X-100. The samples were incubated in this solution at room temperature for 1 h. Following blocking, the buffer was replaced with a 0.1% BSA solution containing Troponin I (Abcam) diluted at 1 : 100. The samples were incubated overnight at 4 °C, then washed with PBS. For secondary antibody labelling, a solution of 0.1% BSA with 1 : 400 secondary antibody (AlexaFluor 488 nm anti-rabbit, Thermo Fisher Scientific) and 1 : 40 AlexaFluor 594 Phalloidin (Thermo Fisher Scientific) was applied, and the samples were incubated at room temperature for 1 h, followed by PBS washes and Hoechst33342 labelling (Thermo Fisher Scientific). Imaging was performed using a confocal fluorescence microscope (FLUOVIEW FV3000, Evident Scientific).

For the experiments presented in the SI, immunostaining was additionally performed using sarcomeric α-actinin (Abcam, 1 : 100), N-cadherin (Sigma-Aldrich, 1 : 100), and DAPI for nuclear staining. Imaging was performed with the Leica SP8 confocal microscope.

Ca^{2+} imaging

HL-1 cells were stained with Fluo-8 AM according to the manufacturer's instructions. Briefly, 200 μL of Fluo-8 AM solution, diluted to a final concentration of 5 μM in Claycomb medium (supplemented as described), was added to the cells, and the cells were incubated for 1 hour. Then, it was washed with PBS once and replaced with fresh medium. Prior to analysis, videos were converted to grayscale, background-subtracted using the temporal average image, and smoothed using a Gaussian filter (radius = 10 pixels, σ = 15). Activation time was defined as the frame at which pixel intensity reached 10% of its maximum value over the recording. Pixels not exceeding 0.5% of the average image intensity were excluded to reduce noise.

Electrophysiological experiments

Electrical recording and stimulation were carried out using an MEA control system (MED64-Basic System, Med Scientific), comprising a main amplifier, head amplifier, and connector. Each MEA was linked to the amplifiers through the connector. Signals were amplified with a gain of 2000 and filtered using a band-pass filter set between 1 and 1000 Hz. The analogue signals were digitised at a sampling rate of 20 kHz. Recordings were performed at 37 °C with 5% CO_2 using a stage-top mini-incubator (TOKAI HIT). The MEA sample was promptly transferred from the culture incubator to the recording mini-incubator and allowed to equilibrate for 10 min before data acqui-

†All animal experiments were approved by the Biological Safety and Ethics Committee of NTT Basic Research Laboratories (approval ID 2025-05), which follow the Guidelines for the Proper Conduct of Animal Experiments of the Science Council of Japan (Kohyo-20-k16-2, 2006).

sition, ensuring environmental stability and minimizing variability in cardiomyocyte activity. To reduce signal noise, a bandpass filter and a notch filter at 50 Hz were implemented in post-processing. For the stimulation experiments, we applied biphasic, current-controlled pulses, with a phase duration of 100 μs. For the experiments presented in the SI, recordings and stimulation were performed using a portable MEA system (MEA2100-Mini-System, Multichannel Systems).

Data analysis

All data processing and analysis were performed in MATLAB (MathWorks), unless otherwise stated.

Results and discussion

Design and fabrication of self-folding graphene electrodes

The fabrication details of the self-foldable graphene electrodes are described in the Experimental section and in previously reported protocols (Fig. 1a).[43–45] Briefly, we first patterned metal feedlines on a glass substrate. Then, we coated and patterned a sacrificial Ca-alginate layer so that it was present only in the areas where the electrodes needed to fold. We used a wet transfer process to transfer the graphene onto the sample and subsequently etched the graphene to separate it into 4 electrodes. After fully laminating the samples with parylene-C and patterning the multi-electrode self-foldable films, we deposited and patterned a second parylene-C layer to serve as passivation of the feedlines. Last, we used an EDTA solution to dissolve Ca-alginate. Upon dissolution of the sacrificial Ca-alginate layer, the patterned structures folded up due to the compressive strain in the parylene-C film introduced during thermal processing.[42]

We integrated 16 micro-rolls with a 1 mm pitch into each sample, yielding 64 electrodes in total (Fig. 1b). For measurements with the MEA2100-Mini-System, 60 electrodes were used. The purpose of this design was to clearly distinguish the cellular organisation in each micro-roll from the surrounding planar area. The spacing between the 4 electrodes in each self-folding scaffold was designed to minimise crosstalk while preserving the micro-roll architecture (Fig. 1c). The geometrical dimensions of each micro-roll-shaped scaffold were chosen to ensure that tissue aggregates remain below the maximum nutrient diffusion length of 3D cell assemblies.[46] While larger tissue constructs are feasible by increasing the micro-roll dimensions and initial cell density, additional strategies such as microfluidic perfusion or vascular co-culture would be necessary to prevent central necrosis. Importantly, the lithographic fabrication approach used here is inherently scalable, allowing the production of large-area arrays containing hundreds of individually addressable micro-rolls. Such array-based configurations could enable high-throughput electrophysiological measurements and systematic pharmacological testing, providing a route toward miniaturised cardiac drug screening platforms. We chose the thickness of the parylene-C layer interfacing with graphene based on previously reported mechanical analyses to predict the resulting curvature radius.[39] For this purpose, we modelled our self-folding graphene electrodes as 4 individual half tubes with a 150 μm perimeter connected by a 100 μm hinge. A front view of this model is illustrated in Fig. 1d. Fig. 1e shows phase-contrast images of the folded graphene micro-rolls in different magnifications. The folding radius was measured for 10 representative micro-rolls per device across 4 different samples (n = 40 total). Across all structures, the radius was 61.8 ± 3.5 μm (mean ± SD), corresponding to a coefficient of variation of ~6%. The device-to-device variation, calculated from the mean radius of each device, was 61.8 ± 2.1 μm (n = 4 devices), indicating high reproducibility of the self-folding process. The deviation from the design target (~50 μm) is primarily attributed to the sensitivity of the rolling curvature to the parylene-C thickness and residual stress during deposition, which becomes difficult to control for films in the ~100 nm range.[42] Despite this variation, the resulting micro-roll height remains within the intended range (~100 μm), and the scaffold geometry is further dynamically adapted by cardiomyocyte contractile forces during tissue formation.

Electrochemical characterisation

Electrochemical characterisation of the graphene micro-roll electrodes was conducted using EIS and CV to assess signal interface quality and charge transfer properties (Fig. 2). The EIS measurements revealed a characteristic frequency-dependent decrease in impedance magnitude across the 1 Hz to 100 kHz range, accompanied by a consistent phase profile. While the overall impedance was higher than in previous designs,[42] this increase is attributed to two key design modifications in the current system: the implementation of a complete passivation layer and the reduction in both the exposed graphene area and its contact interface with the underlying Au feedlines. These changes are critical to ensuring long-term electrode stability and spatial selectivity, particularly when operating in 3D culture environments. The cyclic voltammograms show stable and consistent curves, indicating preserved electrochemical activity and low variability across electrodes. Together, these results confirm that despite the higher impedance, the new electrode architecture supports reliable electrical interfacing while enhancing structural robustness and insulation.

To assess stimulation safety and operational stability of the graphene microelectrodes, we further characterised their electrochemical response under dynamic stimulation conditions. Cyclic voltammetry measurements were first used to determine the electrochemical potential window of the graphene electrodes and define the safe operating limits (Fig. 2c). Within this regime, voltage transient measurements were performed using biphasic current pulses with amplitudes ranging from 10 to 100 μA (Fig. 2d).

By using the maximum cathodic potential excursion (E_{mc}) and the safety limits identified from cyclic voltammetry, we determined the charge injection capacity (CIC) of the electrodes, which measures the maximum amount of electrical charge an electrode can safely deliver into the surrounding

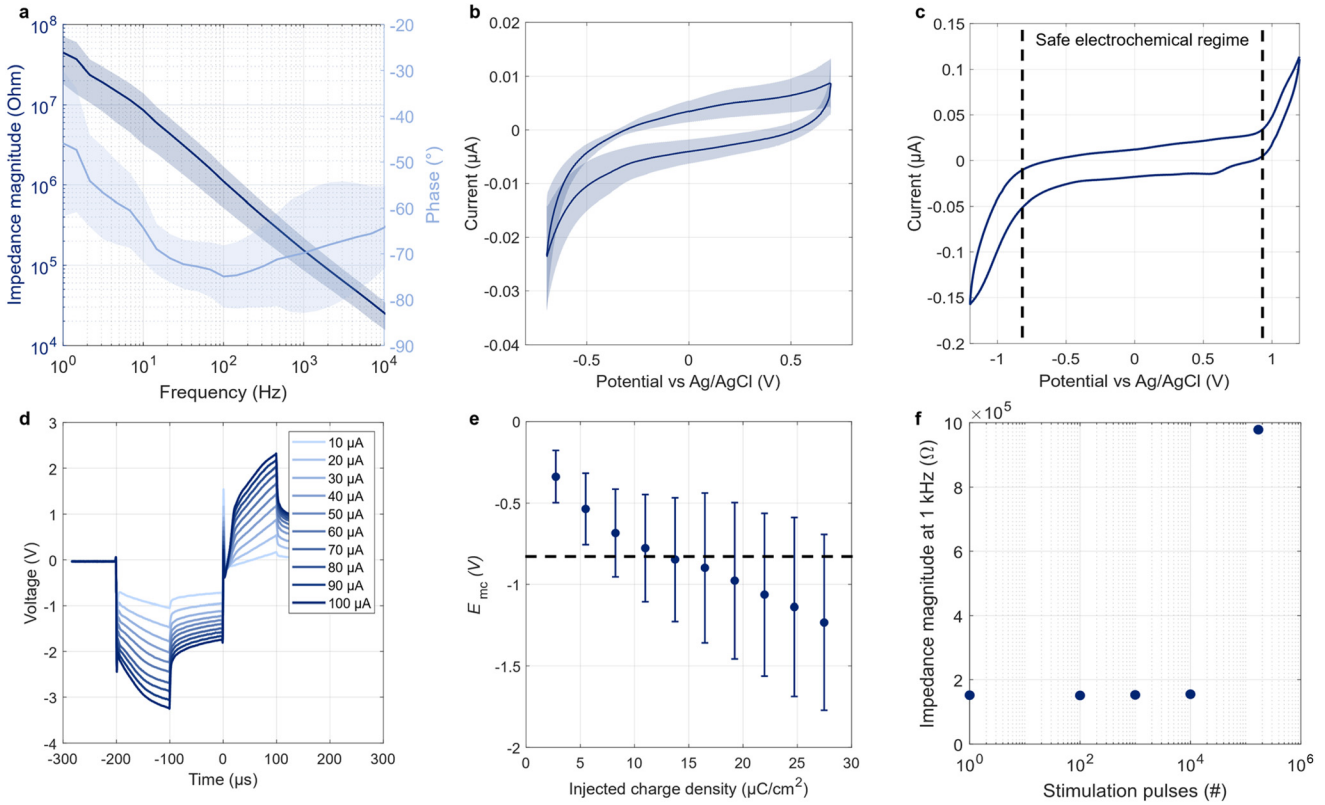

Fig. 2 Electrochemical analysis and stimulation safety assessment of the folded graphene microelectrodes. (a) Impedance spectroscopy plot showing impedance magnitude (blue) and phase (orange) *versus* frequency for 16 representative electrodes; the solid line denotes the mean and the shaded area the standard deviation. (b) Cyclic voltammetry curves displaying the current–voltage response of the same electrodes. (c) Exemplary cyclic voltammetry measurement including the safe electrochemical regime (d) Voltage response to biphasic current pulses of amplitudes between 10–100 μA. All traces are the mean of n = 3 samples. (e) Charge injection capacity (CIC) calculated from the voltage responses (mean and standard deviation of n = 3 samples). We chose the maximum cathodic potential E_{mc} as a metric because of its lower safe electrochemical limit as determined in (c). (f) Stability of the electrode interface during repeated stimulation. The impedance magnitude at 1 kHz was monitored during continuous stimulation pulses, showing stable impedance values for up to 10^4 pulses (mean ± standard deviation, n = 3 electrodes; 1 electrode measured up to >10^5 pulses).

medium without causing irreversible electrochemical reactions (Fig. 2e). The CIC was estimated at around 13 μC cm^{-2}, which is in the order of magnitude typical for monolayer graphene, especially when interfaced with a subjacent Au feedline.[47]

To evaluate the stability of the electrode interface under repeated stimulation, the impedance magnitude at 1 kHz was monitored during continuous pulse application slightly above the safety limit (50 μA) (Fig. 2f). The impedance remained stable over more than 10^4 stimulation pulses, indicating that the graphene electrodes maintain their electrochemical properties under repeated stimulation. No visible side effects such as bubble formation, medium discolouration, or morphological changes to the electrodes were observed during these experiments. However, exceeding this limit by an order of magnitude led to a 10-fold increase in impedance, accompanied by electrode flattening. We attribute this observation to a detachment of monolayer graphene due to prolonged stimulation outside the safety limit. These results give a deeper insight into the stimulation capabilities and limitations of monolayer graphene microelectrodes.

Rolled-up graphene electrodes as cardiac tissue scaffolds

To evaluate the dynamic behaviour of primary cardiomyocytes cultured on graphene micro-rolls, we performed a time-course analysis over 5 days *in vitro* (DIV 5). Phase contrast microscopy (Fig. 3a) revealed progressive morphological changes in the developing cell culture, with initial cell adhesion and spreading observed at DIV 0 and 1, followed by cell aggregation inside the micro-rolls by DIV 2. Notably, a rhythmical movement of the micro-roll edges could be observed, indicating synchronised beating of the cardiomyocytes, possibly facilitated by the graphene's conductive interface, which enhances electrophysiological coupling and gap junction formation in electrically active cells (Movie S1).[48] By DIV 5, the micro-rolls appeared fully encapsulated by a dense multicellular layer, indicating significant tissue assembly following the scaffold shape. In areas with the highest cell density, we also observed interconnecting tissue aggregates bridging individual micro-rolls (Fig. S3), suggesting functional tissue-to-tissue communication.

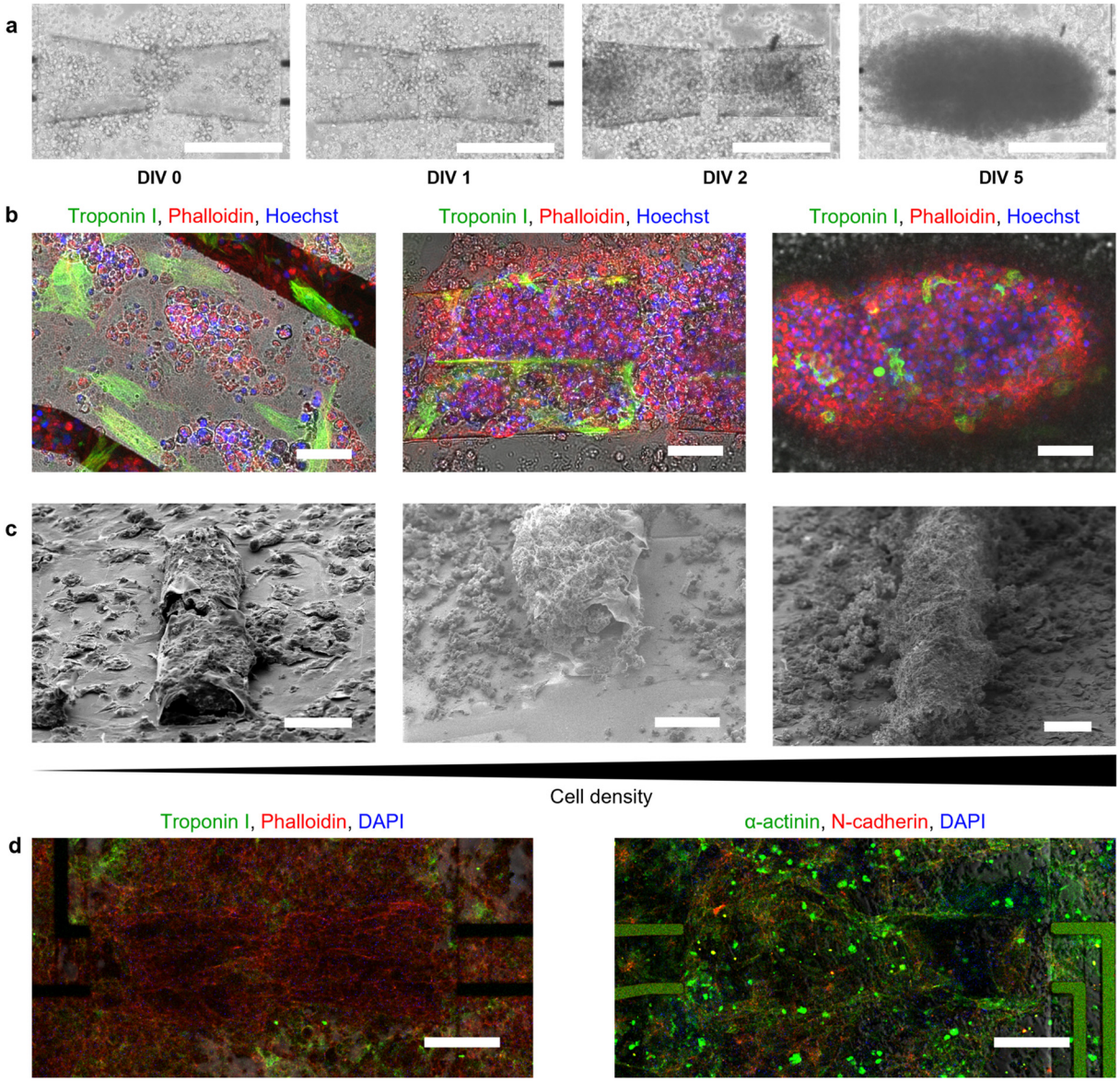

Fig. 3 Morphological, immunofluorescent, and SEM characterisation of cardiomyocytes cultured on graphene micro-rolls. (a) Time-lapsed phase contrast images of primary cardiomyocyte culture on a graphene micro-roll during the first 5 days. (b) Immunostaining images of the primary cardiomyocyte culture at DIV 5 in a flat area (left), low density graphene micro-roll (centre) and high-density graphene micro-roll (right) (c) SEM images of self-folded graphene microelectrodes with increasing cell density from left to right. (d) Exemplary immunostaining images of HL-1 cardiomyocytes at DIV 11 (left) and hiPSC-CMs at DIV 10. Scale bars: (a) 200 μm, (b) 50 μm, (c) 100 μm (left and right), 50 μm (centre). (d) 100 μm.

Unlike previously reported self-folding devices,[16,49–52] our platform not only provides external contact with 3D tissues but also accesses inner areas, allowing for internal electrophysiological measurements. Typically, this requires tissues to be penetrated by stiff electrodes, which introduces a high risk of damage to cellular networks.[53,54] In contrast, our design enables 3D tissues to grow directly around the electrodes, providing a tight electrode–tissue seal without additional mechanical stress, a feature that is crucial to ensure efficient signal coupling.[55,56] The optical transparency of graphene further allows simultaneous high-resolution imaging and electrical readout—an advantage over opaque metal electrodes.[31]

Immunofluorescence staining at DIV 5 provided insight into the cell population (Fig. 3b and Movies S2, S3). Troponin I (green), a marker of cardiomyocyte contractile machinery, was consistently expressed, with prominent localisation on the graphene surface outside of the micro-rolls. This preferential attachment may be attributed to graphene's favourable physicochemical properties and ability to facilitate charge transfer, improving cell attachment and promoting global maturation compared to cells grown on standard surfaces.[57,58] Phalloidin (red) and Hoechst (blue) staining confirmed the presence of actin cytoskeleton and nuclei, respectively, revealing increased overall cellular density inside the rolled structures

compared to the flat surface. Since phalloidin labels F-actin in both cardiomyocytes and cardiac fibroblasts, the elevated signal likely reflects a mixed cell population. These findings suggest that the micro-roll architecture not only facilitates cardiomyocyte aggregation but also supports stromal cell integration, potentially influencing tissue mechanics and electrophysiological coupling. Complementary SEM imaging (Fig. 3c) showed higher levels of cell coverage and surface integration with increasing cell densities. In particular, high-density micro-rolls exhibited a dense, cohesive tissue-like architecture, underscoring the robustness of graphene-based self-folded constructs to support 3D cardiac engineered tissues.

To further assess the compatibility of the graphene micro-roll platform, additional culture experiments were performed with HL-1 and hiPSC-CMs over extended time periods. Time-lapse imaging and immunofluorescence staining up to DIV 10–11 demonstrate stable cell attachment and the formation of organised cardiomyocyte networks on the scaffold (Fig. S4 and S5). Representative immunostaining images from these experiments are also shown in Fig. 3d. Thanks to the high transparency of monolayer graphene, we were also able to perform Ca^{2+} imaging recordings to assess the field potential propagation along the micro-rolls (Movie S4). A corresponding time delay map can be found in Fig. S6.

Electrophysiological recordings

To demonstrate the capability of our graphene micro-roll scaffolds to act as integrated electrodes for electrophysiology monitoring, we recorded the spontaneous electrical activity of the cardiomyocyte culture. A representative trace over 120 s from a single graphene microelectrode (Fig. 4a) showed cyclic extracellular field potentials, indicating currents generated by spontaneous cardiac beating. The corresponding average field potential shape (Fig. 4b) further confirmed the presence of recurring, stereotyped electrical events, with the shaded region denoting the standard deviation across detected field potentials. Electrical recordings across three distinct 4-electrode graphene micro-rolls (Fig. 4c) revealed similar spontaneous activity patterns, underscoring the reproducibility and sensitivity of the platform. The spatial arrangement and colour-coded electrode layout enabled the visualisation of field potential propagation, as can be seen in the magnified view of an example field potential highlighted by the dashed rectangle (Fig. 4d). We quantified the spontaneous beating frequency from field potential recordings, which provides a reliable measure of network rhythmicity and synchrony across electrodes (mean 0.91 ± 0.05 Hz, n = 24 electrodes). These results demonstrate that, despite the high electrochemical impedance, the graphene micro-roll architecture not only supports cardiomyocyte viability and assembly but also enables high-fidelity, multiplexed electrophysiological recording within 3D microenvironments.

Quantitative electro-performance metrics

To quantitatively benchmark the recording performance of the graphene micro-roll electrodes, we performed additional measurements using HL-1 cardiomyocytes, which provide

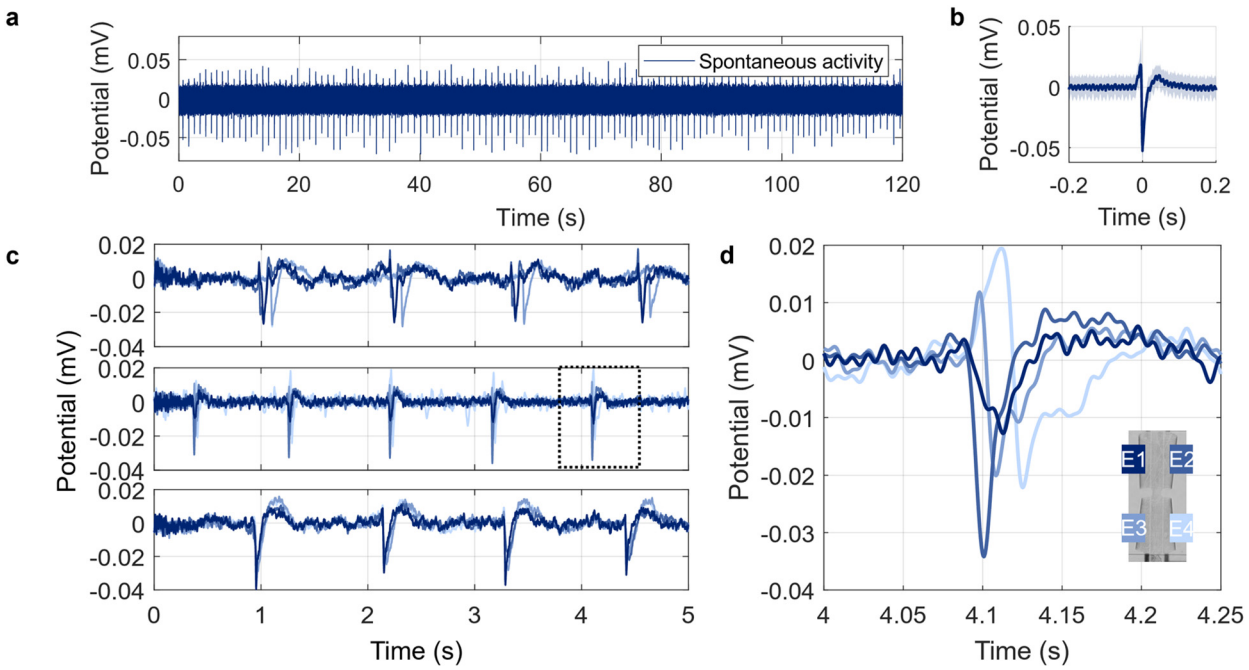

Fig. 4 Spontaneous electrical activity of primary cardiomyocytes measured through the integrated graphene electrodes. (a) Representative raw recording from a single microelectrode over 120 s showing spontaneous field potentials in the absence of external stimulation. (b) Average peak shape of the recording in (a). The shaded area represents the standard deviation. (c) Filtered recordings of the spontaneous electrical activity from three different 4-electrode graphene micro-rolls. Each colour corresponds to an individual electrode of the micro-roll. (d) Magnified view of the dashed rectangle in (c). The colour code for each electrode (E1, E2, E3 and E4) is shown at the bottom right corner.

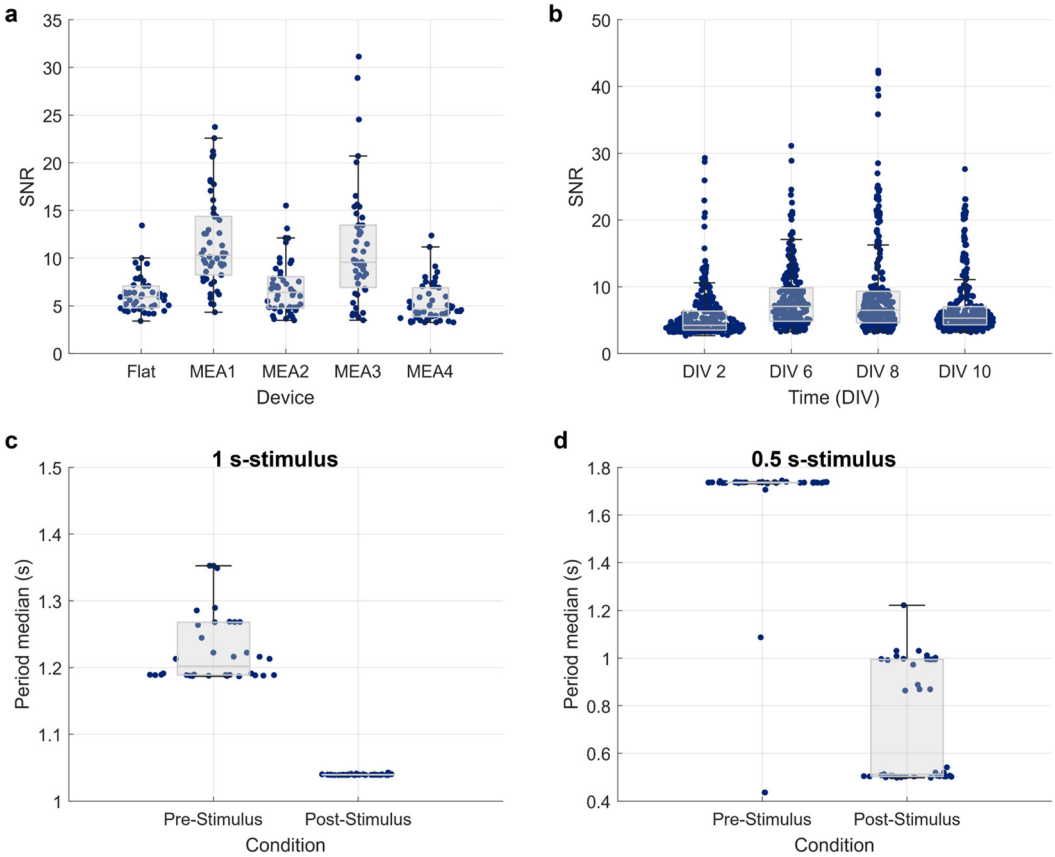

Fig. 5 Quantitative evaluation of recording performance and stimulation-induced modulation using HL-1 cardiomyocytes. (a) SNR across 4 graphene micro-roll MEAs (n = 183 channels in total) and a planar reference (n = 42 channels) at DIV 6, shown as channel-wise swarm plots with boxplot overlays. (b) SNR across all channels from the same 4 micro-roll MEAs as a function of time *in vitro* (DIV 2–10), demonstrating stable recording performance over time. (c) Median beating period before and after a 10 μA, 1 s periodic stimulation, showing alignment with the stimulation interval (n = 38 channels). (d) Median beating period before and after a 60 μA, 0.5 s periodic stimulation, indicating partial synchronisation at the stimulation period (n = 43 channels).

robust and reproducible field potential signals. The signal-to-noise ratio (SNR) was evaluated across multiple devices and compared to a planar reference MEA (Fig. 5a). The micro-roll electrodes exhibit SNR values comparable to or exceeding the planar reference, with some device-to-device variability. Following 50 Hz notch filtering, the SNR was calculated from the single-channel noise floor V_{RMS} and the peak-to-peak field potential amplitude V_{pp} as SNR = $V_{pp}/2V_{RMS}$.

To assess the stability of the recording performance over time, the SNR was monitored across multiple days (DIV 2–10) (Fig. 5b). The results indicate stable signal quality over the investigated period, with a tendency towards increased SNR during the first days, consistent with progressive network maturation. The slight decrease on the final days of measurements is attributed to progressive cell death due to over-confluency of the HL-1 cell population. Noise RMS and field potential amplitude for each individual channel, as well as the percentage of biologically active channels during these experiments, are shown in Fig. S7 and S8.

In addition, the stimulation capability of the graphene micro-rolls was analysed by quantifying the median beating period before and after applying a stimulation pulse train consisting of 10 pulses (summary shown in Fig. 5c and d). In these experiments, stimulation at 1 Hz produced an amplitude-dependent modulation of the beating frequency, where stimulation at 10 μA resulted in transient synchronisation of the beating rhythm to approximately 1 Hz, while no modulation was observed at 5 μA (Fig. S9). Similarly, stimulation at 2 Hz resulted in an entrainment-like response across many electrodes, with beating frequencies approaching the stimulation frequency (Fig. S10). Notably, a subset of channels exhibited synchronised activity at approximately half the stimulation frequency (*i.e.*, responding at every second stimulus pulse), indicating partial entrainment of the network activity.

Proof-of-concept stimulation experiments

To further assess the functional responsiveness of primary cardiomyocytes interfaced with the graphene microelectrode platform, we applied an external periodic electrical stimulus and analysed its impact on spontaneous field potential dynamics. Each stimulation pulse had an amplitude of 50 μA and was repeated 100 times. Continuous recordings from the same

electrode before and after a 2 s periodic stimulus (Fig. S11) revealed changes in the rhythmicity of spontaneous electrical activity. Analysis of the average inter-spike period demonstrated a notable shift towards the stimulus frequency post-stimulation (Fig. 6a), indicating stimulation-induced modulation of the network rhythm. After the first 20 s, the inter-spike interval decreased sharply towards its original value and finally stabilised after ~1 min. Based on this behaviour, we chose a 20 s window to statistically analyse the stimulus effect after stimuli with different periods. The spatial configuration of the 6 analysed electrodes, with electrode #4 serving as the stimulation site (Fig. 6b), enabled assessment of the spatial extent of the stimulation response across the tissue interface. To minimise the impact of potential outliers in the peak detection algorithm, we chose the period median and the median absolute deviation as metrics. Fig. 6c shows the values acquired from 20 s-windows pre- and post-stimulation for 0.5 s, 1 s, 2 s, and 3 s periodic stimuli. The 1 s stimulus modulated the inter-spike periods towards the stimulation frequency and reduced their variability. In contrast, the 0.5 s stimulus did not shift the inter-spike periods towards the stimulation frequency, but it did reduce variability around the 1 s interval, suggesting synchronisation with every second stimulus. This is likely due to the stimulus interval being shorter than the cardiomyocytes'

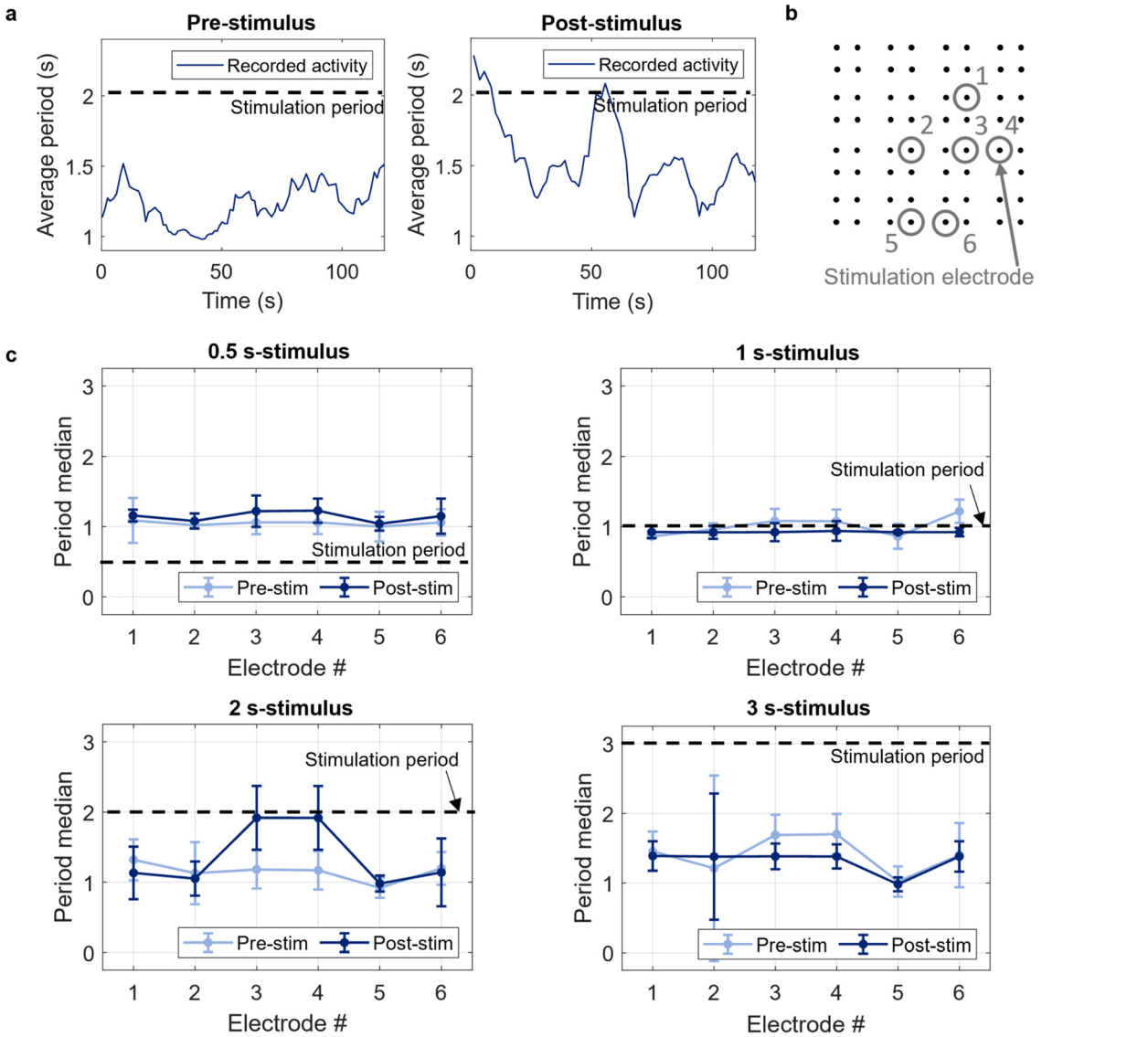

Fig. 6 Stimulation-induced modulation of primary cardiomyocyte activity using integrated graphene microelectrodes. (a) Average inter-spike period before and after applying a 2 s periodic electrical stimulus (indicated by dashed line) to one electrode. (b) Schematic location of the 6 evaluated electrodes in the stimulation experiment. Electrode #4 is the stimulation electrode. (c) Period median of the recorded activity from 6 electrodes during a 20 s time window before and after stimuli. The stimulation period is represented by a dashed line. The error bars represent the median absolute deviation.

effective refractory period. After the 2 s stimulus, only the electrodes closest to the stimulation site followed the imposed pacing, while the others continued beating near the cardiomyocytes' natural rhythm, roughly half the stimulation period. Similarly, the 3 s stimulus shifted the inter-spike periods at the 5 nearest electrodes towards half of the stimulation period. In this case, the external pacing frequency is slow enough to allow spontaneous beats to emerge, resetting the rhythm towards the tissue's intrinsic frequency. The spatial dependence of these responses may also reflect the heterogeneous cellular composition of the cultures. In particular, the presence of myofibroblasts can influence myocardial impulse propagation in a frequency-dependent manner.[59] Collectively, these findings confirm that graphene microelectrodes not only capture spontaneous cardiac electrophysiology but also enable external modulation of network dynamics, thereby offering a controllable platform for studying electro-responsive tissue behaviour.

Conclusions

We introduced a self-folded graphene-based bioelectronic scaffold that integrates structural and functional elements within a single platform for cardiac tissue engineering. The graphene micro-rolls simultaneously act as 3D scaffolds promoting tissue assembly and as active electrical interfaces enabling real-time recording and modulation of cardiomyocyte activity. Future work will focus on increasing the number and spatial distribution of microelectrodes within a single microroll to further enhance the spatiotemporal resolution of signal acquisition and allow for more localised stimulation. In addition, implementing stable long-term pacing protocols will allow investigation of stimulation-induced electromechanical maturation of cardiomyocyte networks on the scaffold, including quantitative analysis of sarcomeric organisation and intercellular coupling during tissue development. Beyond simple rolled geometries, expanding the platform to more complex scaffold designs, such as ring-shaped structures, may better mimic native cardiac architectures and enable the study of more physiologically relevant tissue dynamics. We believe that these advancements will be critical for future bioelectronic platforms to study cardiac development, disease progression, and therapeutic screening within precisely engineered 3D environments.

Author contributions

Alonso Ingar Romero: Conceptualization (lead); Data curation (lead); Formal analysis (lead); Investigation (lead); Methodology (lead); Validation (lead); Visualization (lead); Writing-original draft (lead); Writing-review & editing (lead). Koji Sakai: Conceptualization (lead); Data curation (lead); Formal analysis (lead); Investigation (lead); Methodology (lead); Funding acquisition (equal). Toichiro Goto: Investigation (supporting); Methodology (supporting). George Al Boustani: Data curation (equal); Investigation (supporting); Methodology (supporting). Ryuya Kida: Investigation (supporting); Methodology (supporting). Defne Tüzün: Formal analysis (supporting); Investigation (supporting); Methodology (supporting). Yuta Tanimura: Investigation (supporting); Methodology (supporting). Ann-Caroline Heiler: Investigation (supporting); Methodology (supporting); Writing – original draft (supporting). Joe Alexander: Funding acquisition (lead); Project administration (lead); Writing – review & editing (supporting). Andreas R. Bausch: Investigation (supporting); Methodology (supporting); Project administration (supporting). Bernhard Wolfrum: Funding acquisition (supporting); Project administration (lead); Writing – original draft (lead); Writing – review & editing (lead). Tetsuhiko F. Teshima: Conceptualization (lead); Data curation (supporting); Formal analysis (supporting); Investigation (supporting); Methodology (supporting); Funding acquisition (lead); Project administration (lead); Writing-original draft (lead); Writing-review & editing (lead). The manuscript was written through the contributions of all authors. All authors have given approval to the final version of the manuscript.

Conflicts of interest

There are no conflicts to declare.

Data availability

The data supporting this article have been included as part of the Supplementary Information.

Supplementary information (SI) is available. See DOI: https://doi.org/10.1039/d5nr03812j.

Acknowledgements

We gratefully acknowledge Ms Yuriko Furukawa for assistance with cell culture and Dr Taiki Otomo for assistance with microfabrication. We also thank Mr Philipp Röthlein for support during cleanroom experiments. We thank Mr Benedikt Pfluger for providing a protocol for the cleaning and reuse of MEAs. This study was partially supported by JSPS KAKENHI Grant Number JP25H02631.

References

1 D. Zhang, I. Y. Shadrin, J. Lam, H.-Q. Xian, H. R. Snodgrass and N. Bursac, *Biomaterials*, 2013, **34**, 5813–5820.
2 K. Ronaldson-Bouchard and G. Vunjak-Novakovic, *Cell Stem Cell*, 2018, **22**, 310–324.
3 Y. Zhao, N. Rafatian, N. T. Feric, B. J. Cox, R. Aschar-Sobbi, E. Y. Wang, P. Aggarwal, B. Zhang, G. Conant, K. Ronaldson-Bouchard, A. Pahnke, S. Protze, J. H. Lee,

L. Davenport Huyer, D. Jekic, A. Wickeler, H. E. Naguib, G. M. Keller, G. Vunjak-Novakovic, U. Broeckel, P. H. Backx and M. Radisic, *Cell*, 2019, **176**, 913–927.
4 B. Bhana, R. K. Iyer, W. L. K. Chen, R. Zhao, K. L. Sider, M. Likhitpanichkul, C. A. Simmons and M. Radisic, *Biotechnol. Bioeng.*, 2010, **105**, 1148–1160.
5 R. E. Ahmed, T. Anzai, N. Chanthra and H. Uosaki, *Front. Cell Dev. Biol.*, 2020, **8**, 178.
6 C. M. Kofron and U. Mende, *J. Physiol.*, 2017, **595**, 3891–3905.
7 S. Baghersad, A. Sathish Kumar, M. J. Kipper, K. Popat and Z. Wang, *J. Funct. Biomater.*, 2023, **14**, 269.
8 N. T. Feric and M. Radisic, *Adv. Drug Delivery Rev.*, 2016, **96**, 110–134.
9 Z. Chen, Z. Lin, S. N. Obaid, E. Rytkin, S. A. George, C. Bach, M. Madrid, M. Liu, J. LaPiano, A. Fehr, X. Shi, N. Quirion, B. Russo, H. Knight, A. Aduwari, I. R. Efimov and L. Lu, *Sci. Adv.*, 2023, **9**, eadi0757.
10 J. Haft, *Prog. Cardiovasc. Dis.*, 1974, **16**, 539–568.
11 R. Hinch, *Prog. Biophys. Mol. Biol.*, 2002, **78**, 45–81.
12 M. E. Spira and A. Hai, *Nat. Nanotechnol.*, 2013, **8**, 83–94.
13 D. E. Fullenkamp, W.-Y. Maeng, S. Oh, H. Luan, K. S. Kim, I. A. Chychula, J.-T. Kim, J.-Y. Yoo, C. W. Holgren, A. R. Demonbreun, S. George, B. Li, Y. Hsu, G. Chung, J. Yoo, J. Koo, Y. Park, I. R. Efimov, E. M. McNally and J. A. Rogers, *Sci. Adv.*, 2024, **10**, eado7089.
14 K. Ronaldson-Bouchard, S. P. Ma, K. Yeager, T. Chen, L. Song, D. Sirabella, K. Morikawa, D. Teles, M. Yazawa and G. Vunjak-Novakovic, *Nature*, 2018, **556**, 239–243.
15 F. Zhang, K. Y. Qu, B. Zhou, Y. Luo, Z. Zhu, D. J. Pan, C. Cui, Y. Zhu, M. L. Chen and N. P. Huang, *Biosens. Bioelectron.*, 2021, **179**, 113080.
16 A. Kalmykov, C. Huang, J. Bliley, D. Shiwarski, J. Tashman, A. Abdullah, S. K. Rastogi, S. Shukla, E. Mataev, A. W. Feinberg, K. J. Hsia and T. Cohen-Karni, *Sci. Adv.*, 2019, **5**, eaax0729.
17 D. J. Richards, Y. Li, C. M. Kerr, J. Yao, G. C. Beeson, R. C. Coyle, X. Chen, J. Jia, B. Damon, R. Wilson, E. Starr Hazard, G. Hardiman, D. R. Menick, C. C. Beeson, H. Yao, T. Ye and Y. Mei, *Nat. Biomed. Eng.*, 2020, **4**, 446–462.
18 Q. Lyu, S. Gong, J. G. Lees, J. Yin, L. W. Yap, A. M. Kong, Q. Shi, R. Fu, Q. Zhu, A. Dyer, J. M. Dyson, S. Y. Lim and W. Cheng, *Nat. Commun.*, 2022, **13**, 7259.
19 N. Zhang, F. Stauffer, B. R. Simona, F. Zhang, Z.-M. Zhang, N.-P. Huang and J. Vörös, *Biosens. Bioelectron.*, 2018, **112**, 149–155.
20 D. A. Soscia, D. Lam, A. C. Tooker, H. A. Enright, M. Triplett, P. Karande, S. K. G. Peters, A. P. Sales, E. K. Wheeler and N. O. Fischer, *Lab Chip*, 2020, **20**, 901–911.
21 X. Wang, R. Feiner, H. Luan, Q. Zhang, S. Zhao, Y. Zhang, M. Han, Y. Li, R. Sun, H. Wang, T.-L. Liu, X. Guo, H. Oved, N. Noor, A. Shapira, Y. Zhang, Y. Huang, T. Dvir and J. A. Rogers, *Extreme Mech. Lett.*, 2020, **35**, 100634.
22 S. R. Shin, Y.-C. Li, H. L. Jang, P. Khoshakhlagh, M. Akbari, A. Nasajpour, Y. S. Zhang, A. Tamayol and A. Khademhosseini, *Adv. Drug Delivery Rev.*, 2016, **105**, 255–274.
23 S. Pilato, S. Moffa, G. Siani, F. Diomede, O. Trubiani, J. Pizzicannella, D. Capista, M. Passacantando, P. Samorì and A. Fontana, *ACS Appl. Mater. Interfaces*, 2023, **15**, 14077–14088.
24 S. R. Shin, S. M. Jung, M. Zalabany, K. Kim, P. Zorlutuna, S. b. Kim, M. Nikkhah, M. Khabiry, M. Azize, J. Kong, K.-t. Wan, T. Palacios, M. R. Dokmeci, H. Bae, X. Tang and A. Khademhosseini, *ACS Nano*, 2013, **7**, 2369–2380.
25 P. Hitscherich, A. Aphale, R. Gordan, R. Whitaker, P. Singh, L.-h. Xie, P. Patra and E. J. Lee, *J. Biomed. Mater. Res., Part A*, 2018, **106**, 2923–2933.
26 N. Jalilinejad, M. Rabiee, N. Baheiraei, R. Ghahremanzadeh, R. Salarian, N. Rabiee, O. Akhavan, P. Zarrintaj, A. Hejna, M. R. Saeb, A. Zarrabi, E. Sharifi, S. Yousefiasl and E. N. Zare, *Bioeng. Transl. Med.*, 2023, **8**, e10347.
27 Q. Huang, T. Deng, W. Xu, C. Yoon, Z. Qin, Y. Lin, T. Li, Y. Yang, M. Shen, S. M. Thon, J. B. Khurgin and D. H. Gracias, *Adv. Intell. Syst.*, 2020, **5**, eabq5031.
28 W. Xu, Z. Qin, C.-T. Chen, H. R. Kwag, Q. Ma, A. Sarkar, M. J. Buehler and D. H. Gracias, *Sci. Adv.*, 2017, **3**, e1701084.
29 T. F. Teshima, C. S. Henderson, M. Takamura, Y. Ogawa, S. Wang, Y. Kashimura, S. Sasaki, T. Goto, H. Nakashima and Y. Ueno, *Nano Lett.*, 2019, **19**, 461–470.
30 H. Gao, Z. Wang, F. Yang, X. Wang, S. Wang, Q. Zhang, X. Liu, Y. Sun, J. Kong and J. Yao, *Nat. Commun.*, 2024, **15**, 2321.
31 D. Kuzum, H. Takano, E. Shim, J. C. Reed, H. Juul, A. G. Richardson, J. de Vries, H. Bink, M. A. Dichter, T. H. Lucas, D. A. Coulter, E. Cubukcu and B. Litt, *Nat. Commun.*, 2014, **5**, 5259.
32 L. H. Hess, M. Jansen, V. Maybeck, M. V. Hauf, M. Seifert, M. Stutzmann, I. D. Sharp, A. Offenhäusser and J. A. Garrido, *Adv. Mater.*, 2011, **23**, 5045–5049.
33 A. Savchenko, D. Kireev, R. T. Yin, I. R. Efimov and E. Molokanova, *Front. Bioeng. Biotechnol.*, 2023, **11**, 1168667.
34 D. Kireev, M. Brambach, S. Seyock, V. Maybeck, W. Fu, B. Wolfrum and A. Offenhäusser, *Sci. Rep.*, 2017, **7**, 6658.
35 D. Kireev, S. Kutagulla, J. Hong, M. N. Wilson, M. Ramezani, D. Kuzum, J.-H. Ahn and D. Akinwande, *Nat. Rev. Mater.*, 2024, **9**, 906–922.
36 M. Dankerl, M. V. Hauf, A. Lippert, L. H. Hess, S. Birner, I. D. Sharp, A. Mahmood, P. Mallet, J.-Y. Veuillen, M. Stutzmann and J. A. Garrido, *Adv. Funct. Mater.*, 2010, **20**, 3117–3124.
37 L. H. Hess, M. Seifert and J. A. Garrido, *Proc. IEEE*, 2013, **101**, 1780–1792.
38 J. Kang, D. Shin, S. Bae and B. H. Hong, *Nanoscale*, 2012, **4**, 5527–5537.
39 K. Sakai, T. F. Teshima, T. Goto, H. Nakashima and M. Yamaguchi, *Adv. Funct. Mater.*, 2023, **33**, 2301836.
40 T. Teshima, H. Onoe, K. Kuribayashi-Shigetomi, H. Aonuma, K. Kamiya, H. Ishihara, H. Kanuka and S. Takeuchi, *Small*, 2014, **10**, 912–921.
41 X. Lian, J. Zhang, S. M. Azarin, K. Zhu, L. B. Hazeltine, X. Bao, C. Hsiao, T. J. Kamp and S. P. Palecek, *Nat. Protoc.*, 2013, **8**, 162–175.

42 A. Ingar Romero, T. Raicevic, G. Al Boustani, M. Gupta, A.-C. Heiler, L. Bichlmaier, M. Barbone, M. Becherer, D. Kiriya, S. Inoue, J. Alexander, K. Müller, A. R. Bausch, B. Wolfrum and T. F. Teshima, *ACS Appl. Mater. Interfaces*, 2025, **17**, 10305–10315.
43 K. Sakai, T. F. Teshima, H. Nakashima and Y. Ueno, *Nanoscale*, 2019, **11**, 13249–13259.
44 K. Sakai, S. Miura, T. F. Teshima, T. Goto, S. Takeuchi and M. Yamaguchi, *Nanoscale Horiz.*, 2023, **8**, 1529–1536.
45 T. Goto, T. F. Teshima, K. Sakai and M. Yamaguchi, *AIP Adv.*, 2022, **12**, 075002.
46 J. Rouwkema, B. F. J. M. Koopman, C. A. V. Blitterswijk, W. J. A. Dhert and J. Malda, *Biotechnol. Genet. Eng. Rev.*, 2009, **26**, 163–178.
47 B. Koerbitzer, P. Krauss, C. Nick, S. Yadav, J. J. Schneider and C. Thielemann, *2D Mater.*, 2016, **3**, 024004.
48 V. Martinelli, G. Cellot, A. Fabbro, S. Bosi, L. Mestroni and L. Ballerini, *Front. Physiol.*, 2013, **4**, 239.
49 E. Martinelli, O. Akouissi, L. Liebi, I. Furfaro, D. Maulà, N. Savoia, A. Remy, L. Nikles, A. Roux, L. Stoppini and S. P. Lacour, *Sci. Adv.*, 2024, **10**, eadp8054.
50 Y. Park, C. K. Franz, H. Ryu, H. Luan, K. Y. Cotton, J. U. Kim, T. S. Chung, S. Zhao, A. Vazquez-Guardado, D. S. Yang, K. Li, R. Avila, J. K. Phillips, M. J. Quezada, H. Jang, S. S. Kwak, S. M. Won, K. Kwon, H. Jeong, A. J. Bandodkar, M. Han, H. Zhao, G. R. Osher, H. Wang, K. Lee, Y. Zhang, Y. Huang, J. D. Finan and J. A. Rogers, *Sci. Adv.*, 2021, **7**, eabf9153.
51 Q. Huang, B. Tang, J. C. Romero, Y. Yang, S. K. Elsayed, G. Pahapale, T. J. Lee, I. E. Morales Pantoja, F. Han, C. Berlinicke, T. Xiang, M. Solazzo, T. Hartung, Z. Qin, B. S. Caffo, L. Smirnova and D. H. Gracias, *Sci. Adv.*, 2022, **8**, eabq5031.
52 A. Ingar Romero, Q. Jin, K. K. Parker, J. Alexander, B. Wolfrum and T. F. Teshima, *Adv. Intell. Syst.*, 2024, **6**, 2400055.
53 L. Luan, X. Wei, Z. Zhao, J. J. Siegel, O. Potnis, C. A. Tuppen, S. Lin, S. Kazmi, R. A. Fowler, S. Holloway, A. K. Dunn, R. A. Chitwood and C. Xie, *Sci. Adv.*, 2017, **3**, e1601966.
54 E. Fernández, B. Greger, P. A. House, I. Aranda, C. Botella, J. Albisua, C. Soto-Sánchez, A. Alfaro and R. A. Normann, *Front. Neuroeng.*, 2014, **7**, 24.
55 P. Fromherz, A. Offenhäusser, T. Vetter and J. Weis, *Science*, 1991, **252**, 1290–1293.
56 A. Stett, U. Egert, E. Guenther, F. Hofmann, T. Meyer, W. Nisch and H. Haemmerle, *Anal. Bioanal. Chem.*, 2003, **377**, 486–495.
57 J. Wang, C. Cui, H. Nan, Y. Yu, Y. Xiao, E. Poon, G. Yang, X. Wang, C. Wang, L. Li, K. R. Boheler, X. Ma, X. Cheng, Z. Ni and M. Chen, *ACS Appl. Mater. Interfaces*, 2017, **9**, 25929–25940.
58 T. Kim, Y. H. Kahng, T. Lee, K. Lee and D. H. Kim, *Mol. Cells*, 2013, **36**, 577–582.
59 Y. Tsuji, T. Ogata, K. Mochizuki, S. Tamura, Y. Morishita, T. Takamatsu, S. Matoba and H. Tanaka, *Front. Physiol.*, 2024, **15**, 1352911.